Biochemistry

Article

Cite This: Biochemistry 2018, 57, 3641−3649

pubs.acs.org/biochemistry

Cooperative Assembly of Hsp70 Subdomain Clusters

Maya A. Wright,[†,∥] Francesco A. Aprile,[†] Mathias M. J. Bellaiche,[†,‡] Thomas C. T. Michaels,[†,§] Thomas Müller,[†,∥] Paolo Arosio,[⊥] Michele Vendruscolo,[†] Christopher M. Dobson,[†] and Tuomas P. J. Knowles*[,†,#]

[†]Department of Chemistry, University of Cambridge, Lensfield Road, Cambridge CB2 1EW, U.K.

[‡]Laboratory of Chemical Physics, National Institute of Diabetes and Digestive and Kidney Diseases, National Institutes of Health, Bethesda, Maryland 20892, United States

[§]Paulson School of Engineering and Applied Sciences, Harvard University, Cambridge, Massachusetts 02138, United States

[∥]Fluidic Analytics Ltd., Cambridge, U.K.

[⊥]Institute for Chemical and Bioengineering, ETH Zurich, Vladimir-Prelog-Weg 1, ETH Hönggerberg, HCI F 105, 8093 Zurich, Switzerland

[#]Cavendish Laboratory, Department of Physics, University of Cambridge, JJ Thomson Avenue, Cambridge CB3 0HE, U.K.

Supporting Information

ABSTRACT: Many molecular chaperones exist as oligomeric complexes in their functional states, yet the physical determinants underlying such self-assembly behavior, as well as the role of oligomerization in the activity of molecular chaperones in inhibiting protein aggregation, have proven to be difficult to define. Here, we demonstrate direct measurements under native conditions of the changes in the average oligomer populations of a chaperone system as a function of concentration and time and thus determine the thermodynamic and kinetic parameters governing the self-assembly process. We access this self-assembly behavior in real time under native-like conditions by monitoring the changes in the micrometer-scale diffusion of the different complexes in time and space using a microfluidic platform. Using this approach, we find that the oligomerization mechanism of the Hsp70 subdomain occurs in a cooperative manner and involves structural constraints that limit the size of the species formed beyond the limits imposed by mass balance. These results illustrate the ability of microfluidic methods to probe polydisperse protein self-assembly in real time in solution and to shed light on the nature and dynamics of oligomerization processes.

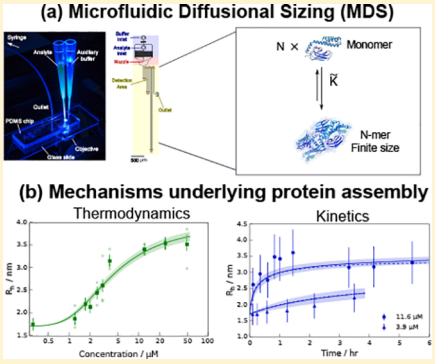

Molecular chaperones play a crucial role *in vivo* not only in assisting in protein folding but also in regulating the formation of aberrant protein assemblies, including in particular those implicated in the onset and progression of neurodegenerative disorders such as Alzheimer's and Parkinson's diseases.[1−9] Despite their important cellular roles, defining the microscopic mechanisms by which molecular chaperones can protect against pathogenic aggregation remains a substantial challenge to study as a result of the polydispersity of the systems involved.[10−13] Indeed, many molecular chaperones, including the 70 kDa heat shock proteins (Hsp70s) and small heat shock proteins such as αB-crystallin, are known to have the propensity to self-assemble into various oligomeric forms, and it has been thought that this serves as a control mechanism for storage of chaperones when they are not exerting their cellular functions.[12,14−29] Evaluating the intrinsic dynamics of molecular chaperones in the presence and absence of their interaction partners is therefore a key target in biophysical studies to begin to define the specific oligomeric species responsible for the suppression of protein aggregation.

A number of conventional biophysical techniques are currently available for probing the quaternary structure and oligomeric populations of proteins; these approaches, however, are typically more reliable for monodisperse solutions of isolated components.[14,30−32] Moreover, many of the techniques involve the interaction of the protein of interest with a surface or a matrix, which may influence the self-assembly behavior. It has recently become apparent, however, that microfluidic techniques offer a fruitful avenue for the characterization of the dynamics, interactions, and physical properties of biomolecules in solution.[8,9,16,33−39] These approaches include methods for the rapid sizing of biological complexes in solution by monitoring the spatiotemporal evolution of their diffusion through a microfluidic channel.[39−41] In this work, we have applied microfluidic diffusional sizing (MDS) to the study of the oligomerization of SBD641, the substrate binding subdomain (residues 384−641) of human Hsp70. Construct

Received: February 7, 2018
Revised: May 12, 2018
Published: May 15, 2018

DOI: 10.1021/acs.biochem.8b00151
Biochemistry 2018, 57, 3641−3649

SBD641 consists of the hydrophobic linker, the substrate binding subdomain itself, and the helical lid, which are the regions that have been found to be critical for oligomerization in full-length Hsp70.[14] We show that the rapid nature of the microfluidic sizing measurements under native solution conditions makes this approach particularly important for quantitative studies of the kinetics as well as the thermodynamics of oligomerization processes. In particular, we demonstrate a robust method for determining the dissociation constant, oligomerization free energy, and association and dissociation rate constants of the self-assembly reaction and show that the assembly process is guided by specific structural constraints and is qualitatively different from unconstrained polymerization processes.

MATERIALS AND METHODS

Protein Expression and Purification. SBD641 was purified according to a protocol outlined previously.[42] In brief, *N*-hexa-His-tagged SBD641 was expressed recombinantly in *Escherichia coli* from the pET28b (Novagen) vector. The cells were then centrifuged, resuspended in buffer [50 mM Tris (pH 7.4)], and lysed using sonication. The expressed protein was collected using a Ni^{2+}-NTA Superflow column (Qiagen, Manchester, U.K.) using standard washing procedures. The protein was further purified by size exclusion chromatography using a Superdex 75 26/60 column (GE Healthcare, Buckinghamshire, UK).

Labeling. Alexa Fluor 488 (Life Technologies, Paisley, UK) was added to SBD641 (10 mM Tris, pH 7.4) at a 1:2 Alexa:SBD641 molar ratio and degassed. The samples labeled at 1:2 and 1:5 ratios were used in the experiments for SBD641 concentrations below and above 3 μM, respectively. The mixture was left to incubate overnight in the dark at 4 °C. The excess dye was removed after 24 h of incubation using a Zeba Spin desalting column 7 kDa (Thermo Scientific, Cramlington, UK) followed by size exclusion chromatography with a Superdex 10/300 GL column (GE Healthcare Life Sciences, Amersham). The protein was then divided into aliquots, flash-frozen, and stored at −80 °C until further use.

Microfluidic Device Fabrication. The microfluidic devices used in this study were fabricated using standard soft-lithography techniques.[43] SU-8 3025 photoresist (3 mL, MicroChemCorp, Westborough, MA) was spin-coated onto a silicon wafer at 3000 rpm to create 25 μm height channels. After being baked at 96 °C for 12 min, the wafers were covered with a photomask imprinted with a pattern of the device. The wafer was then exposed to ultraviolet (UV) radiation for 15 s at an intensity of 16 mW/cm^2 (OAI Instruments, San Jose, CA) and baked at 96 °C for a further 5 min. This procedure allowed cross-linking of the photoresist in the regions exposed to UV light, and the residual photoresist was then removed with PGMEA (propylene glycol methyl ether acetate). The master was subsequently rinsed with IPA (isopropyl alcohol) and dried.

The PDMS (polydimethylsiloxane) curing agent and elastomer (Dow Corning) were thoroughly mixed in a 1:10 ratio. Carbon black nanopowder (Sigma-Aldrich, Dorset, U.K.) was added to the mixture, which was subsequently centrifuged for 5 min at 5000 rpm to spin down large clusters of carbon powder. The centrifuged black PDMS was then poured into a Petri dish containing the wafer, and the dish was placed in a vacuum desiccator for 30 min to eliminate air bubbles and then baked at 65 °C for 3 h.

Diffusion Measurements. The microfluidic devices were plasma bonded to glass microscope slides using an Electronic Femto Plasma Bonder (Diener, Ebhausen, Germany) directly before use. The channels in the bonded device were filled from the outlet with the relevant buffer using a 250 or 500 μL glass syringe (Hamilton Robotics, Bonaduz, GR, Switzerland), needles (25 gauge, 0.5 mm × 16 mm) (Neolus Terumo, Bagshot, U.K.), and polyethene tubing (inner diameter of 0.38 mm, outer diameter of 1.09 mm). The sample and buffers were loaded into their respective device inlets using gel loading pipet tips.

Fluid flow through the device was controlled using neMESYS syringe pumps (Cetoni GmbH, Korbussen, Germany) at a flow rate of 100 or 160 μL/h. Once the system had equilibrated, the diffusion profiles were imaged using an inverted fluorescence microscope (Zeiss Axio Observer.D1) fitted with broadband white LED illumination (Cairn Research, Faversham, U.K.) and a 49002 GFP filter (Chroma Technology, Bellows Falls, VT). The microfluidic diffusion channels were imaged at 12 points along the channels using an Evolve 512 CCD camera (Photometrics, Tuscon, AZ) with a 10× objective and exposure times ranging from 1 to 10 s depending on the sample concentration.

Numerical Simulations and Data Analysis for Microfluidic Sizing Experiments. Fitting of the basis functions to the experimental data was performed as described previously.[39] The basis functions used in this analysis were simulated in the range of radii relevant to the samples, namely, 0.25−10 nm in 0.25 nm increments.[44]

Fluidity One Measurements. In addition, we used a Fluidity One (Fluidic Analytics Ltd., Cambridge, U.K.), which is a self-contained instrument that enables microfluidic diffusional sizing measurements with post separation labeling using injection moulded disposable plastic chips, rather than PDMS. Four repeats were taken on 10 μL of unlabeled SBD641 at 0.3 μM on a prototype instrument.

Thermodynamic Models of SBD641 Oligomerization. *Model with No Cooperativity.* Assuming a single equilibrium constant K for the association and dissociation of monomers, the equilibrium concentration $[A_j]$ of j-mers is given by[45]

$$[A_j] = K^{-1}(K[A_1])^j \tag{1}$$

where the equilibrium monomer concentration $[A_1]$ is linked to the total concentration of protein molecules $[A]_{tot}$ through mass conservation, yielding:

$$K[A_1] = \frac{1 + 2K[A]_{tot} - \sqrt{1 + 4K[A]_{tot}}}{2K[A]_{tot}} \tag{2}$$

Using eq 1, we obtain the average hydrodynamic radius at equilibrium

$$\bar{R} = R_m \frac{\sum_{j=1}^{\infty} j^{d^{-1}+1}[A_j]}{\sum_{j=1}^{\infty} j[A_j]} = \frac{R_m}{K[A]_{tot}} \mathrm{Li}_{-(d+1)}\left(\frac{1 + 2K[A]_{tot} - \sqrt{1 + 4K[A]_{tot}}}{2K[A]_{tot}}\right) \tag{3}$$

where $\mathrm{Li}_s(z) = \sum_{k=1}^{\infty} z^k/k^s$ is the polylogarithm function of order s, R_m is the size of the pure monomer, and d is the fractal

DOI: 10.1021/acs.biochem.8b00151
Biochemistry 2018, 57, 3641−3649

dimension governing the dependence of aggregate size on polymerization number $R_j = j^{d^{-1}} R_m$.

Negative Cooperativity. Assuming an association−dissociation equilibrium constant $K = K_0/j$, we obtain the following expression for the concentration of filaments of size j at equilibrium

$$[A_j] = \frac{K_0^{-1}}{j!}(K_0[A_1])^j \tag{4}$$

where a relationship between the equilibrium monomer concentration and the total concentration of protein molecules is given in terms of the Lambert W-function $K_0[A_1] = W(K_0[A]_{tot})$. Thus, the dependence of the average hydrodynamic radius on the total protein concentration becomes

$$\bar{R} = \frac{R_m}{K_0[A]_{tot}} \sum_{j=1}^{\infty} \frac{j^{d^{-1}}[W(K_0[A]_{tot})]^j}{(j-1)!} \tag{5}$$

Positive Cooperativity with a Size Limit. This model assumes a monomer−N equilibrium, with a very fast pre-equilibrium between intermediates. The overall equilibrium is a result of several distinct steps in a more detailed model in which monomers are sequentially added to N-mers. At low values of N, we note that intermediate populations can start to emerge. Using the equilibrium concentration of oligomers $[A_N] = \tilde{K}[A_1]^N$, we obtain for the average hydrodynamic radius

$$\bar{R} = \frac{R_m}{[A]_{tot}}([A_1] + N^{d^{-1}+1}\tilde{K}[A_1]^N) \tag{6}$$

where the total concentration dependence of equilibrium monomer concentration $[A_1]$ is found by inverting the mass balance equation $[A_{tot}] = [A_1] + N\tilde{K}[A_1]^N$.

Kinetics. These rate laws assume that N-mers are the largest oligomers formed and that the time evolution is given by

$$\frac{d[A_N](t)}{dt} = k_a[A_1](t)^N - k_-[A_N](t) \tag{7}$$

$$\frac{d[A_1](t)}{dt} = -N\frac{d[A_N](t)}{dt} \tag{8}$$

where $[A_1](t)$ and $[A_N](t)$ are the monomer and N-mer concentrations at time t, respectively.

The time evolution of the hydrodynamic radius, then, is obtained from a mole-fraction weighted average of the radius of each species:

$$R_h = \frac{R_m}{[A_1](0)}[[A_1](t) + N^{d^{-1}+1}[A_N](t)] \tag{9}$$

Note that the kinetic equations (eqs 7 and 8) emerge from a steady-state approximation of a more detailed model that assumes N-mers to be formed by the addition of individual monomers in sequence with rate constant $k_+^{(i)}$:

$$\frac{d[A_2](t)}{dt} = k_+^{(1)}[A_1]^2 - k_-[A_2](t)$$

$$\frac{d[A_3](t)}{dt} = k_+^{(2)}[A_1](t)[A_2](t) - k_-[A_3](t)$$

$$\vdots$$

$$\frac{d[A_N](t)}{dt} = k_+^{(N-1)}[A_1](t)[A_{N-1}](t) - k_-[A_N](t)$$

The connection between association rate constant k_a entering eqs 7 and 8 and the geometrically averaged elongation rate constant $\langle k_+ \rangle = [k_+^{(1)}k_+^{(2)}k_+^{(3)}]^{1/3}$, assuming size-independent dissociation rate constants, is given by (for $N = 4$)

$$k_a = \frac{k_+^{(1)}k_+^{(2)}k_+^{(3)}}{k_-^2} \tag{10}$$

$$k_a = \frac{\langle k_+ \rangle^3}{k_-^2} \tag{11}$$

Using the measured values for k_a and equilibrium constant $\tilde{K} = (\langle k_+ \rangle/k_-)^3 = k_a/k_-$, we could determine the elongation rate constant to be approximately $\langle k_+ \rangle = 2.0 \pm 1.2\ M^{-1}\ s^{-1}$. This elongation rate corresponds to an association reaction whose barrier is the arithmetic mean of those for dimer, trimer, and tetramer formation through monomer addition, assuming similar diffusive prefactors for all.

Data Fitting. We assumed in all cases that $R_m = 1.7$ nm, the R_h value obtained at the lowest concentration of SBD641 measured.

In the case of the fits to models without and with negative cooperativity, we minimized the $\chi^2 = \sum_i \sigma_i^{-2}[y_i - f(x_i;\mathbf{p})]^2$ between the thermodynamic data and each model with respect to the parameters $\alpha = d^{-1}$ and the relevant equilibrium constant. Here y_i is the measured hydrodynamic radius corresponding to initial concentration x_i, and $\mathbf{p}$ is a vector of the parameters. We took as a constant estimate for the error σ_i the average non-zero standard deviation of hydrodynamic radii, averaged over all the initial concentrations.

For the two-state model, we performed a global fit to the thermodynamic and kinetic data simultaneously by minimizing the sum of kinetic and thermodynamic contributions to total χ^2 with respect to the elements of parameter vector $\mathbf{p} = (\alpha,\tilde{K},k_a)$. The errors in each kinetic data point were taken as 20% of the measured values. The derivation of the target function to minimize can be found in the Supporting Information. Note that off rate k_- was constrained by k_a and the association constant $\tilde{K}$ by applying detailed balance: $\tilde{K} = k_a/k_-$. To sample rate constant space exponentially, the exponent (base 10) of the on rate constant k_a was fitted.

In practice, all fits were performed by using the basinhopping algorithm of Python's scipy module, which involves several minimization steps interspersed by random moves in parameter space and effectively samples glassy fitting landscapes by removing barriers between local and global minima.[46] The minimization scheme was an L-BFGS-B algorithm implemented in Python's scipy.minimize module.[47] To avoid non-physical regimes, the parameters of the no- or negative-cooperativity models were constrained to the regions $0 \le \alpha \le 1$ and $K \ge 0$. For the two-state fits, the imposed bounds were $k_a \ge 0$, $\tilde{K} \ge 1$, and $0 \le \alpha \le 1 \times 10^{-18}$.

DOI: 10.1021/acs.biochem.8b00151
Biochemistry 2018, 57, 3641−3649

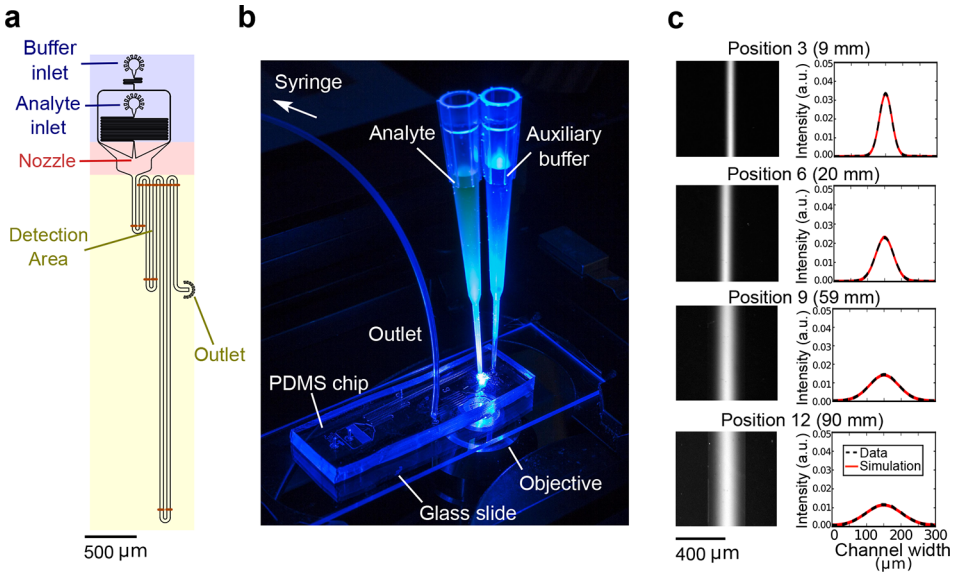

Figure 1. Overview of the approach for the rapid micrometer-scale diffusion measurements used for sizing biological complexes used in this work. (a) Schematic diagram of the microfluidic device, showing in brown the positions at which the mass distributions are measured. (b) Picture of a microfluidic diffusion device during measurement illuminated by blue light from an inverted fluorescence microscope. The tips connected to the device contain the analyte and an auxiliary buffer, which are drawn through the device by applying a low pressure at the outlet of the device by means of a syringe pump. (c) Diffusion profiles (left) of 24 μM SBD641 (in 10 mM Tris buffer at pH 7.4) at specific positions along the diffusion channel. The distances traveled by the analyte with respect to the nozzle are shown above each image. Lateral scans (right) of the diffusion profiles (dotted lines) fitted to a simulated set of basis functions (red lines). The extent of diffusion at each distance is dependent on the hydrodynamic radii of the molecular species present.

Errors in the fitted parameters were estimated by building an approximate covariance matrix of χ^2 and propagated to the fits as described in the Supporting Information.[48] Following minimization, α was converted to scaling exponent d, using the equation $d = \alpha^{-1}$, with errors propagated in the standard way.

RESULTS

Multidimensional Microfluidic Diffusion Measurements. We measured the diffusion coefficients of SBD641 in solution by monitoring lateral diffusion under steady-state laminar flow in a microfluidic channel using a device shown schematically in Figure 1a.[39] The cysteine residues of SBD641 were conjugated to an AlexaFluor488 dye for visualization of the sample diffusion profiles, and images were taken at 12 different positions under steady-state flow conditions using the experimental procedure shown in Figure 1b. The diffusion profiles acquired in this way were then fitted to a linear combination of simulated basis functions calculated for ideal monodisperse solutions[44] (Figure 1c), yielding the average diffusion coefficients of the particles in the solution.[37,39,49]

Thermodynamics of Oligomerization of the Hsp70 Substrate Binding Subdomain. To explore the thermodynamic determinants of SBD641 self-assembly, we determined the average hydrodynamic radius R_h of the SBD641 construct in solution at 12 different monomer concentrations between 0.3 and 50 μM using the microfluidic diffusion approach described above. Each measurement was repeated two to four times at flow rates of 100 and 160 μL/h in at least two devices fabricated independently. We found that the average R_h values increased significantly with concentration, from 1.8 ± 0.2 nm at 0.3 μM to 3.41 ± 0.15 nm at 12 μM, at which concentration the radius appeared to plateau (Figure 2a). The increase in the radius indicates an elevated population of higher-order oligomers with an increasing SBD641 concentration, in accordance with results from bulk experiments.[14] In addition, to verify that the fluorescent label does not affect the measured hydrodynamic radii of SBD641, we performed sizing measurements at 0.3 μM unlabeled protein using a Fluidic Analytics Fluidity One instrument. This approach for microfluidic diffusional sizing is based on postseparation labeling.[38] We found the radius of unlabeled SBD641 at 0.3 μM [10 mM sodium phosphate buffer (pH 7.4)] to be 1.89 ± 0.25 nm, in agreement with our labeled construct (Figure 2, blue data point).

To evaluate the thermodynamic parameters governing the oligomerization process, we explored the extent to which the experimental data could be described by different equilibrium models with varying levels of cooperativity (details of each model can be found in Materials and Methods) (Figure 2). The average hydrodynamic radius obtained in the experimental measurements was converted to the number of monomers (j) in individual oligomeric species by means of the relationship $R_j = R_0\sqrt[d]{j}$, where R_j is the hydrodynamic radius of an oligomer with j subunits, R_0 is the hydrodynamic radius of the monomeric species, and d indicates the dimensionality of the cluster (see the Supporting Information).

To understand the role of cooperativity in the assembly of these truncated Hsp70 clusters, we first considered the Oosawa model of equilibrium linear polymerization.[45,51,52] This model does not display any cooperativity because the polymerization reaction is assumed to proceed through simple addition and removal of individual subunits to existing aggregates; moreover, a single equilibrium constant K describes monomer association and dissociation at each polymerization step. Figure 2a shows the best fit of our thermodynamic data to this simple model. Evidently, this model does not account for the key features of the experimental data set; in particular, the fit fails to capture

DOI: 10.1021/acs.biochem.8b00151
Biochemistry 2018, 57, 3641−3649

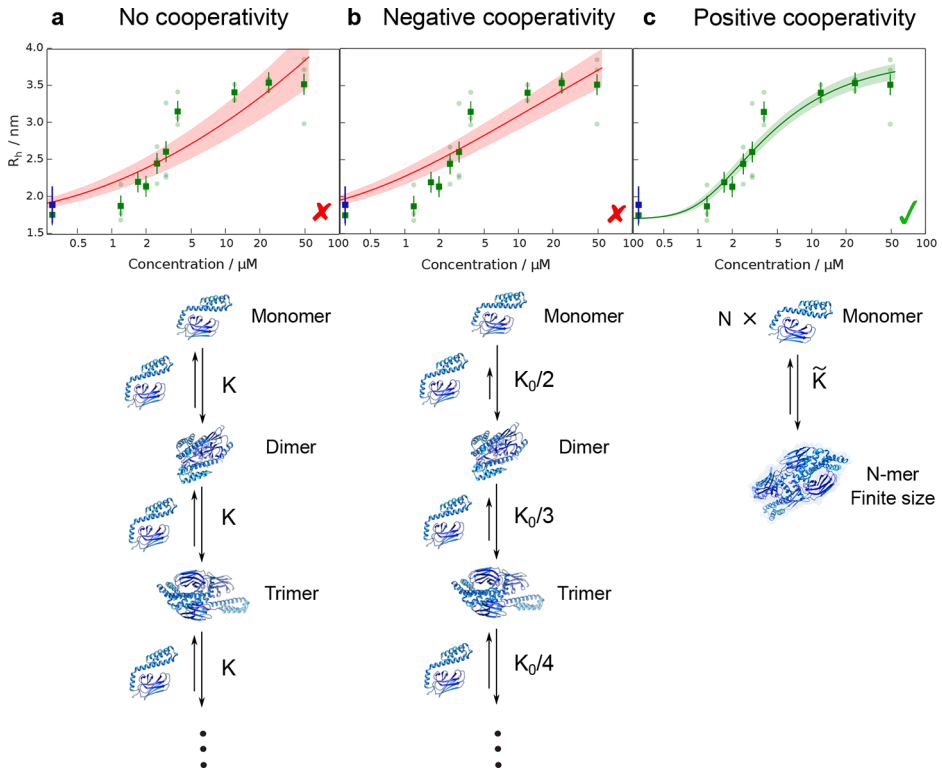

Figure 2. Analysis of the self-assembly behavior of the labeled SBD641 construct. In each case, the circles show the raw experimental data and the opaque green squares show the averaged data with error bars as the average standard deviations, averaged over all concentrations. The opaque blue squares show the average size of the unlabeled construct measured at 0.3 μM. Colored lines (red or green) show the fits to each model, and the shaded regions correspond to the error of each fit. (a) Oosawa model (no cooperativity),[45] in which oligomers of infinite size are allowed to form. The fit yields an association constant K of 1.4 ± 0.6 μM^{-1} and a fractal dimension d of 3.2 ± 0.3. (b) Kinetic limit model (negative cooperativity),[50] where the formation of larger oligomers is limited by the increasing rates of dissociation of the monomer from oligomeric clusters of increasing subunit numbers. The following parameters were obtained from the fit: K_0 = 1.7 ± 0.6 μM^{-1}, and d = 1.80 ± 0.13. (c) Positive cooperativity model, in which the largerst oligomer is capped to N = 4 subunits and a monomer−tetramer equilibrium is assumed (see Materials and Methods). The following parameters were obtained in the best fit: $\tilde{K}$ = 0.035 ± 0.011 μM^{-3}, and d = 1.69 ± 0.06.

the steep transition in oligomer size that occurs at the lowest concentrations measured (Figure 2a).

Because a simple polymerization model without cooperativity is unable to describe the data, we next investigated whether, at the next level of complexity, a polymerization model in which the formation of larger oligomers becomes increasingly less favorable as the size increases could result in a greater level of agreement between the simulation and the experimental data. We therefore examined a model for negative cooperativity in which the dissociation rate of larger clusters increases in proportion to their size,[50] yielding a limit to oligomer size. As for the Oosawa model, the negative cooperativity model assumes that aggregation proceeds by the addition and removal of single subunits, but the equilibrium constant varies with the number of subunits (j) in an oligomer in proportion to $K_j = K_0/j$ for $j > 1$, thus making the formation of larger oligomers less favorable. Despite a slight improvement in the residuals of the fit, this model also fails to capture accurately the behavior of the experimental data under these conditions (Figure 2b).

Because the Oosawa and negative cooperativity models are incapable of capturing the sharp increase in the average R_h values observed in the experiments, we explored a positive cooperativity model by allowing for a higher-than-linear dependence of the rate of oligomer formation on monomer concentration. In the simplest scenario, this effect can be captured by assuming the formation of oligomers of a maximal size of N = 4 subunits, which is the largest oligomeric assembly reported in the literature,[14] from the interaction of multiple monomers. Figure 2c shows that the best fit of the experimental data to this positive cooperativity model yields overall good agreement, demonstrating the necessity of a higher-than-linear monomer concentration dependence of oligomer formation to explain the observed sharp increase in R_h. Similar thermodynamic models in which the subunits demonstrate high positive cooperativity with a limiting oligomer size have been shown to describe protein self-assembly very well in systems that exhibit strong structural constraints, such as the assembly of viral capsids.[53] The best fit to our data under our experimental conditions yields a value for the association constant $\tilde{K}$ of 0.035 ± 0.011 μM^{-3}, i.e., an effective dissociation constant $K_D = \tilde{K}^{-1/3}$ = 3.1 ± 0.3 μM. The effective K_D value determined in this study is broadly consistent with the value reported in the literature, 5−10 μM, for SBD641.[14] We find, moreover, from the measurement of the equilibrium constants that the oligomerization process is thermodynamically favorable with a standard free energy change ($\Delta G^{\ominus}_{assembly}$) of −95.0 ± 0.8 kJ/mol under standard conditions. Our results show therefore that the assembly process of the SBD641 oligomers is highly cooperative with a limit to the maximum size. Moreover, our analysis shows that the limit in the oligomer size at high concentrations is unlikely to originate from purely kinetic constraints, as is the case for instance with linear protein aggregation,[54] but rather appears to have an origin in structural

DOI: 10.1021/acs.biochem.8b00151
Biochemistry 2018, 57, 3641−3649

constraints that counterbalance the thermodynamic driving force for forming larger aggregates at higher concentrations.

Kinetics of Oligomerization of the Hsp70 Substrate Binding Subdomain. We next demonstrate that the microfluidics-based strategy presented here allows us to probe directly the kinetics of self-assembly processes. To this effect, we probed SBD641 oligomerization by measuring the time taken for a purely monomeric sample to re-establish completely the dynamic equilibrium distributions of monomers and oligomers; an aliquot of the monomeric SBD641 was therefore purified by size exclusion chromatography, and the variation in average hydrodynamic radius as a function of time was monitored using MDS at different time points. The cooperativity of the oligomerization process meant that the reassembly started immediately after the fraction of monomers eluted from the column. We conducted measurements for monomeric SBD641 at concentrations of 3.9 and 11.6 μM in 10 mM Tris-HCl buffer (pH 7.4) and found that in both cases the average R_h value of SBD641 increases with time, indicating that the SBD641 oligomerization process is reversible on the time scales of this experiment and that the monomers are able to reassemble into higher-order oligomers (Figure 3), in accord with previous experiments performed in bulk.[14]

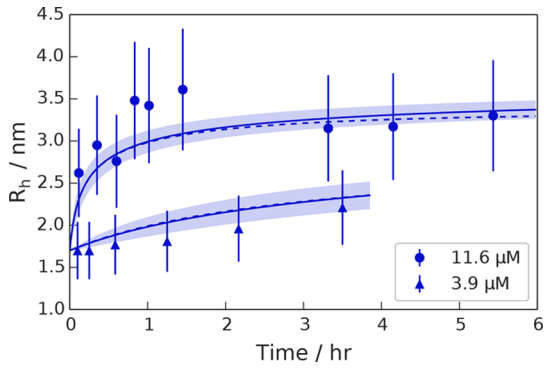

Figure 3. Microfluidic kinetic data obtained for SBD641 at two different concentrations [3.9 μM (triangles) and 11.6 μM (circles)]. The lines show fits of the data to the structural limit model in which the largest oligomer size present in the system is capped to $N_{max} = 4$. Dashed and solid lines show the numerical and analytical approximate solutions to the kinetics, respectively, and shaded regions indicate the error in the fit (details of error analysis in the Supporting Information).

We fitted the microfluidic data obtained at two different initial chaperone concentrations (3.9 and 11.6 μM) to the integrated rate law that captures the kinetics of the positive cooperative aggregation model that was found to describe this system most effectively in our thermodynamic study. Details of the fitting can be found in Materials and Methods. Using this approach, for the self-assembly of the substrate binding subdomain of Hsp70, we obtained an association rate constant k_a of $(2.1 \pm 1.2) \times 10^{11}$ M^{-3} s^{-1} and a dissociation rate constant k_- of $(6 \pm 4) \times 10^{-6}$ s^{-1}. The association rate constant can be further decomposed into an average elongation rate constant per monomer addition step of $\langle k_+ \rangle = 2.0 \pm 1.2$ M^{-1} s^{-1} (see Materials and Methods).

DISCUSSION

Using the results of the kinetic fit, we compared the value of the average elongation rate constant $\langle k_+ \rangle$ obtained here for this truncated molecular chaperone system to that of a variety of self-assembling biomolecular systems, as shown in Figure 4 and Table S2. The self-assembly of the proteins shown in the graph has a variety of biological effects, including proteins such as actin and tubulin that have evolved to aggregate as a part of their function (magenta),[55−57] the molecular chaperone αB-crystallin that is known to form native quaternary structures (green), and non-evolved proteins whose filamentous forms are associated with pathological aggregation such as Aβ_{40}, Aβ_{42}, α-synuclein, insulin, hemoglobin, and the yeast prion protein Ure2p (cyan).[57−64] We find that the geometrically averaged elongation rate constant of the substrate binding subdomain of Hsp70 (red) is much lower than that of most other proteins of biological interest that are known to self-assemble, and that the average elongation rate obtained for our system compares well with that of αB-crystallin, another ubiquitous molecular chaperone, which also forms oligomers (Figure 4 and Table S2). This fits with the trend that is apparent from Figure 4, in which the aggregation rates of nonfilamentous (red and green) structures that form native quaternary assemblies do so more slowly than misfolded, filamentous proteins do (magenta and cyan). The slow average rate of monomer addition of the labeled subdomain of Hsp70 suggests that at least one of the reactions on pathway to aggregate formation is highly unfavorable, and that there is a high activation barrier in the self-assembly process.

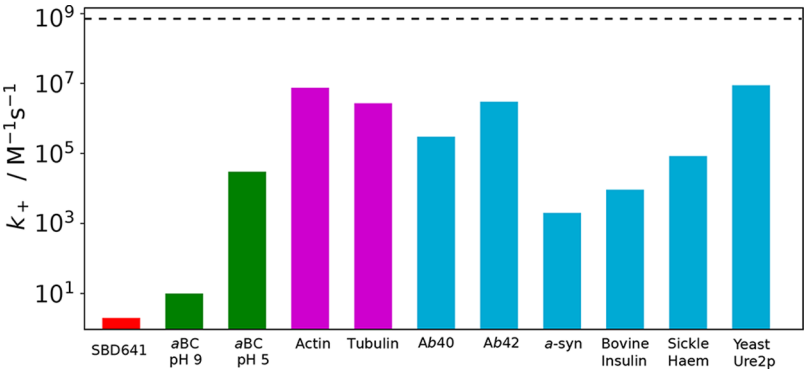

Figure 4. Comparison of the elongation rate constants of various proteins to that of SBD641 (red bar). Green bars indicate nonfilamentous structures, magenta bars evolved filamentous structures, and cyan bars pathological filamentous structures. The dashed line represents diffusion-limited aggregation, which is the limiting value that is physically possible to observe in solution.

DOI: 10.1021/acs.biochem.8b00151
Biochemistry 2018, 57, 3641−3649

CONCLUSIONS

In this study, we have developed a microfluidic approach for determining the values of the thermodynamic parameters governing the oligomerization of proteins under native solution conditions, in particular the dissociation constant and free energy of oligomerization, and have shown that these results can provide novel molecular insights into the mechanisms of the self-assembly process. For the system of truncated human Hsp70 studied here, the analysis of the thermodynamic data reveals that there are strong structural constraints on the size of the oligomers, which are most likely to be determined by specific molecular interaction modes at the oligomerization interface.

In addition, we took advantage of the short analysis times afforded by our microfluidic diffusion measurements, a feature that is crucial for determining the characteristic time scales associated with the rapid assembly of proteins, to show that this method can also be used to determine the overall association rate constant of oligomerization and extract the maximum assembly size. We have shown that the solution-state measurements ensure that we can observe the self-assembly behavior of proteins without compromising oligomer assembly by the interference of a surface as in many other techniques. We anticipate that the approach discussed in this work will provide the opportunity for further quantitative real-time studies of the structure and oligomerization of other self-assembling protein systems of key physiological relevance under native solution conditions.

ASSOCIATED CONTENT

Supporting Information

The Supporting Information is available free of charge on the ACS Publications website at DOI: 10.1021/acs.biochem.8b00151.

Integrated rate law for HSP70 assembly kinetics, maximum likelihood target function for simultaneous fitting, error analysis, and a summary of fit results and comparison of elongation rates of various proteins (PDF)

AUTHOR INFORMATION

Corresponding Author

*E-mail: tpjk2@cam.ac.uk.

ORCID

Francesco A. Aprile: 0000-0002-5040-4420
Paolo Arosio: 0000-0002-2740-1205
Michele Vendruscolo: 0000-0002-3616-1610
Tuomas P. J. Knowles: 0000-0002-7879-0140

Funding

The research leading to these results has received funding from the European Research Council under the European Union's Seventh Framework Programme (FP7/2007-2013) through ERC Grant PhysProt (Agreement 337969) (T.P.J.K., M.A.W., and T.C.T.M.). In addition, the authors are grateful for financial support from the Frances and Augustus Newman Foundation (T.P.J.K. and M.A.W.), the Marie Curie Fellowship scheme (P.A.), the Cambridge Commonwealth, European and International Trust (M.M.J.B.), the NIH-Oxford Cambridge Scholars Programme (M.M.J.B.), St John's College Cambridge (T.C.T.M.), Peterhouse College Cambridge (T.C.T.M.), the Swiss National Science Foundation (T.C.T.M.), and the Biotechnology and Biological Sciences Research Council (T.M.). F.A.A. is supported by a Senior Research Fellowship award from the Alzheimer's Society, UK (Grant 317, AS-SF-16-003). This work was supported in part by the Intramural Research Program of the National Institute of Diabetes and Digestive and Kidney Diseases at the National Institutes of Health (M.M.J.B.) and the Centre for Misfolding Diseases (Cambridge, U.K.).

Notes

The authors declare the following competing financial interest(s): Part of the work described here was done in collaboration with Fluidic Analytics Ltd., of which M.A.W. and T.M. are employees, P.A. is a share holder, C.M.D. is a scientific adviser, and T.P.J.K. is a board member.

REFERENCES

(1) Hartl, F. U., Bracher, A., and Hayer-Hartl, M. (2011) Molecular chaperones in protein folding and proteostasis. *Nature 475*, 324−332.

(2) Hartl, F. U., and Hayer-Hartl, M. (2002) Molecular chaperones in the cytosol: from nascent chain to folded protein. *Science 295*, 1852−1858.

(3) Evans, C. G., Wisén, S., and Gestwicki, J. E. (2006) Heat shock proteins 70 and 90 inhibit early stages of amyloid beta-(1−42) aggregation in vitro. *J. Biol. Chem. 281*, 33182−33191.

(4) Huang, C., Cheng, H., Hao, S., Zhou, H., Zhang, X., Gao, J., Sun, Q.-H., Hu, H., and Wang, C.-C. (2006) Heat shock protein 70 inhibits alpha-synuclein fibril formation via interactions with diverse intermediates. *J. Mol. Biol. 364*, 323−336.

(5) Klucken, J., Shin, Y., Masliah, E., Hyman, B. T., and McLean, P. J. (2004) Hsp70 Reduces alpha-Synuclein Aggregation and Toxicity. *J. Biol. Chem. 279*, 25497−25502.

(6) Luk, K. C., Mills, I. P., Trojanowski, J. Q., and Lee, V. M.-Y. (2008) Interactions between Hsp70 and the hydrophobic core of alpha-synuclein inhibit fibril assembly. *Biochemistry 47*, 12614−12625.

(7) Lashuel, H. A., Hartley, D., Petre, B. M., Walz, T., and Lansbury, P. T. (2002) Amyloid pores from pathogenic mutations. *Nature 418*, 291.

(8) Arosio, P., Michaels, T. C. T., Linse, S., Månsson, C., Emanuelsson, C., Presto, J., Johansson, J., Vendruscolo, M., Dobson, C. M., and Knowles, T. P. J. (2016) Kinetic analysis reveals the diversity of microscopic mechanisms through which molecular chaperones suppress amyloid formation. *Nat. Commun. 7*, 10948.

(9) Aprile, F. A., Arosio, P., Fusco, G., Chen, S. W., Kumita, J. R., Dhulesia, A., Tortora, P., Knowles, T. P. J., Vendruscolo, M., Dobson, C. M., and Cremades, N. (2017) Inhibition of alpha-Synuclein Fibril Elongation by Hsp70 Is Governed by a Kinetic Binding Competition between alpha-Synuclein Species. *Biochemistry 56*, 1177−1180.

(10) De Los Rios, P., and Barducci, A. (2014) Hsp70 chaperones are non-equilibrium machines that achieve ultra-affinity by energy consumption. *eLife 3*, No. e02218.

(11) Freiden, P. J., Gaut, J. R., and Hendershot, L. M. (1992) Interconversion of three differentially modified and assembled forms of BiP. *EMBO J. 11*, 63−70.

(12) Thompson, A. D., Bernard, S. M., Skiniotis, G., and Gestwicki, J. E. (2012) Visualization and functional analysis of the oligomeric states of Escherichia coli heat shock protein 70 (Hsp70/DnaK). *Cell Stress Chaperones 17*, 313−327.

(13) Preissler, S., Chambers, J. E., Crespillo-Casado, A., Avezov, E., Miranda, E., Perez, J., Hendershot, L. M., Harding, H. P., and Ron, D. (2015) Physiological modulation of BiP activity by trans-protomer engagement of the interdomain linker. *eLife 4*, e08961.

(14) Aprile, F. A., Dhulesia, A., Stengel, F., Roodveldt, C., Benesch, J. L. P., Tortora, P., Robinson, C. V., Salvatella, X., Dobson, C. M., and Cremades, N. (2013) Hsp70 oligomerization is mediated by an interaction between the interdomain linker and the substrate-binding domain. *PLoS One 8*, No. e67961.

DOI: 10.1021/acs.biochem.8b00151
Biochemistry 2018, 57, 3641−3649

(15) Gao, B., Eisenberg, E., and Greene, L. (1996) Enzymology: Effect of Constitutive 70-kDa Heat Shock Protein Polymerization on Its Interaction with Protein Substrate Effect of Constitutive 70-kDa Heat Shock Protein Polymerization on Its Interaction with Protein Substrate. *J. Biol. Chem. 271*, 16792−16797.
(16) Angelidis, C. E., Lazaridis, I., and Pagoulatos, G. N. (1999) Aggregation of hsp70 and hsc70 in vivo is distinct and temperature-dependent and their chaperone function is directly related to non-aggregated forms. *Eur. J. Biochem. 259*, 505−512.
(17) Benaroudj, N., Batelier, G., Triniolles, F., and Ladjimi, M. M. (1995) Self-Association of the Molecular Chaperone HSC70t. *Biochemistry 34*, 15282−15290.
(18) Peschek, J., Braun, N., Franzmann, T. M., Georgalis, Y., Haslbeck, M., Weinkauf, S., and Buchner, J. (2009) The eye lens chaperone alpha-Crystallin forms defined globular assemblies. *Proc. Natl. Acad. Sci. U. S. A. 106*, 13272−13277.
(19) Stengel, F., Baldwin, A. J., Painter, A. J., Jaya, N., Basha, E., Kay, L. E., Vierling, E., Robinson, C. V., and Benesch, J. L. P. (2010) Quaternary dynamics and plasticity underlie small heat shock protein chaperone function. *Proc. Natl. Acad. Sci. U. S. A. 107*, 2007−2012.
(20) Stengel, F., Baldwin, A. J., Bush, M. F., Hilton, G. R., Lioe, H., Basha, E., Jaya, N., Vierling, E., and Benesch, J. L. P. (2012) Dissecting heterogeneous molecular chaperone complexes using a mass spectrum deconvolution approach. *Chem. Biol. 19*, 599−607.
(21) Jacobs, W. M., Knowles, T. P. J., and Frenkel, D. (2016) Oligomers of Heat-Shock Proteins: Structures That Don't Imply Function. *PLoS Comput. Biol. 12*, e1004756.
(22) Smirnova, E., Chebotareva, N., and Gurvits, B. (2013) Transient transformation of oligomeric structure of alpha-Crystallin during its chaperone action. *Int. J. Biol. Macromol. 55*, 62−68.
(23) Bova, M. P., Ding, L.-L., Fung, B. K., and Horwitz, J. (1997) Subunit Exchange of α A-Crystallin. *J. Biol. Chem. 272*, 29511−29517.
(24) Feil, I. K., Malfois, M., Hendle, J., van Der Zandt, H., and Svergun, D. I. (2001) A novel quaternary structure of the dimeric alpha-Crystallin domain with chaperone-like activity. *J. Biol. Chem. 276*, 12024−12029.
(25) Hochberg, G. K. A., Ecroyd, H., Liu, C., Cox, D., Cascio, D., Sawaya, M. R., Collier, M. P., Stroud, J., Carver, J. A., Baldwin, A. J., Robinson, C. V., Eisenberg, D. S., Benesch, J. L. P., and Laganowsky, A. (2014) The structured core domain of αB-Crystallin can prevent amyloid fibrillation and associated toxicity. *Proc. Natl. Acad. Sci. U. S. A. 111*, E1562−E1570.
(26) Saha, S., and Das, K. P. (2004) Relationship between chaperone activity and oligomeric size of recombinant human alphaA- and alphaB-Crystallin: a tryptic digestion study. *Proteins: Struct., Funct., Genet. 57*, 610−617.
(27) Horwitz, J., Huang, Q., and Ding, L. (2004) The native oligomeric organization of alpha-Crystallin, is it necessary for its chaperone function? *Exp. Eye Res. 79*, 817−821.
(28) Augusteyn, R. C. (2004) Dissociation is not required for alpha-Crystallin's chaperone function. *Exp. Eye Res. 79*, 781−784.
(29) Hilton, G. R., Hochberg, G. K. A., Laganowsky, A., McGinnigle, S. I., Baldwin, A. J., and Benesch, J. L. P. (2013) C-terminal interactions mediate the quaternary dynamics of αB-Crystallin. *Philos. Trans. R. Soc., B 368*, 20110405.
(30) Burmann, B. M., and Hiller, S. (2015) Chaperones and chaperone-substrate complexes: Dynamic playgrounds for NMR spectroscopists. *Prog. Nucl. Magn. Reson. Spectrosc. 86*−*87*, 41−64.
(31) Jehle, S., Rajagopal, P., Bardiaux, B., Markovic, S., Kühne, R., Stout, J. R., Higman, V. A., Klevit, R. E., van Rossum, B.-J., and Oschkinat, H. (2010) Solid-state NMR and SAXS studies provide a structural basis for the activation of alphaB-Crystallin oligomers. *Nat. Struct. Mol. Biol. 17*, 1037−1042.
(32) Wright, M. A., Aprile, F. A., Arosio, P., Vendruscolo, M., Dobson, C. M., and Knowles, T. P. J. (2015) Biophysical approaches for the study of interactions between molecular chaperones and protein aggregates. *Chem. Commun. 51*, 14425−14434.
(33) Sia, S. K., and Whitesides, G. M. (2003) Microfluidic devices fabricated in poly(dimethylsiloxane) for biological studies. *Electrophoresis 24*, 3563−3576.
(34) Herling, T. W., Arosio, P., Müller, T., Linse, S., and Knowles, T. P. J. (2015) A microfluidic platform for quantitative measurements of effective protein charges and single ion binding in solution. *Phys. Chem. Chem. Phys. 17*, 12161−12167.
(35) Horrocks, M. H., Rajah, L., Jönsson, P., Kjaergaard, M., Vendruscolo, M., Knowles, T. P. J., and Klenerman, D. (2013) Single-Molecule Measurements of Transient Biomolecular Complexes through Microfluidic Dilution. *Anal. Chem. 85*, 6855−6859.
(36) Srisa-art, M., Kang, D., Hong, J., Park, H., Leatherbarrow, R. J., Edel, J. B., Chang, S. I., and DeMello, A. J. (2009) Analysis of Protein - Protein Interactions by Using Droplet-Based Microfluidics. *ChemBioChem 10*, 1605−1611.
(37) Kamholz, A. E., and Yager, P. (2001) Theoretical analysis of molecular diffusion in pressure-driven laminar flow in microfluidic channels. *Biophys. J. 80*, 155−160.
(38) Yates, E. V., Müller, T., Rajah, L., De Genst, E. J., Arosio, P., Linse, S., Vendruscolo, M., Dobson, C. M., and Knowles, T. P. J. (2015) Latent analysis of unmodified biomolecules and their complexes in solution with attomole detection sensitivity. *Nat. Chem. 7*, 802−809.
(39) Arosio, P., Müller, T., Rajah, L., Yates, E. V., Aprile, F. A., Zhang, Y., Cohen, S. I. A., White, D. A., Herling, T. W., De Genst, E. J., Linse, S., Vendruscolo, M., Dobson, C. M., and Knowles, T. P. J. (2016) Microfluidic Diffusion Analysis of the Sizes and Interactions of Proteins under Native Solution Conditions. *ACS Nano 10*, 333−341.
(40) Hatch, A., Kamholz, A. E., Hawkins, K. R., Munson, M. S., Schilling, E. A., Weigl, B. H., and Yager, P. (2001) A rapid diffusion immunoassay in a T-sensor. *Nat. Biotechnol. 19*, 461−465.
(41) Hatch, A., Garcia, E., and Yager, P. (2004) Diffusion-based analysis of molecular interactions in microfluidic devices. *Proc. IEEE 92*, 126−139.
(42) Roodveldt, C., Bertoncini, C. W., Andersson, A., van der Goot, A. T., Hsu, S.-T., Fernández-Montesinos, R., de Jong, J., van Ham, T. J., Nollen, E. A., Pozo, D., Christodoulou, J., and Dobson, C. M. (2009) Chaperone proteostasis in Parkinson's disease: stabilization of the Hsp70/alpha-synuclein complex by Hip. *EMBO J. 28*, 3758−3770.
(43) Qin, D., Xia, Y., and Whitesides, G. M. (2010) Soft lithography for micro- and nanoscale patterning. *Nat. Protoc. 5*, 491−502.
(44) Müller, T., Arosio, P., Rajah, L., Cohen, S. I., Yates, E. V., Vendruscolo, M., Dobson, C. M., and Knowles, T. P. J. (2016) Particle-based simulations of steady-state mass transport at high Péclet numbers. *Int. J. Nonlinear Sci. Numer. Simul. 17*, 175−183.
(45) Oosawa, F., and Asakura, S. (1975) *Thermodynamics of the Polymerization of Protein*, Academic Press.
(46) Wales, D., and Doye, J. P. K. (1997) Global Optimization by Basin-Hopping and the Lowest Energy Structures of Lennard-Jones Clusters Containing up to 110 Atoms. *J. Phys. Chem. A 101*, 5111−5116.
(47) Zhu, C., Byrd, R., Lu, P., and Nocedal, J. (1997) L-BFGS-B: Fortran subroutines for large-scale bound-constrained optimization. *ACM Transactions on Mathematical Software 23*, 550−560.
(48) Richter, P. (1995) Estimating Errors in Least-Squares Fitting. *TDA Progress Reports 42*−*122*, 107−137.
(49) Culbertson, C. T., Jacobson, S. C., and Ramsey, M. J. (2002) Diffusion coefficient measurements in microfluidic devices. *Talanta 56*, 365−373.
(50) Baldwin, A. J., Lioe, H., Robinson, C. V., Kay, L. E., and Benesch, J. L. P. (2011) αB-Crystallin polydispersity is a consequence of unbiased quaternary dynamics. *J. Mol. Biol. 413*, 297−309.
(51) Oosawa, F., and Kasai, M. (1962) A theory of linear and helical aggregations of macromolecules. *J. Mol. Biol. 4*, 10−21.
(52) Cohen, S. I. A., Vendruscolo, M., Dobson, C. M., and Knowles, T. P. J. (2012) From Macroscopic Measurements to Microscopic Mechanisms of Protein Aggregation. *J. Mol. Biol. 421*, 160−171.

DOI: 10.1021/acs.biochem.8b00151
Biochemistry 2018, 57, 3641−3649

(53) Morozov, A. Y., Bruinsma, R. F., and Rudnick, J. (2009) Assembly of viruses and the pseudo-law of mass action. *J. Chem. Phys. 131*, 155101.
(54) Michaels, T. C. T., Lazell, H. W., Arosio, P., and Knowles, T. P. J. (2015) Dynamics of protein aggregation and oligomer formation governed by secondary nucleation. *J. Chem. Phys. 143*, 054901.
(55) Kuhn, J. R., and Pollard, T. D. (2005) Real-time measurements of actin filament polymerization by total internal reflection fluorescence microscopy. *Biophys. J. 88*, 1387−1402.
(56) Engelborghs, Y., de Maeyer, L. C., and Overbergh, N. (1977) A kinetic analysis of the assembly of microtubules in vitro. *FEBS Lett. 80*, 81−85.
(57) Langelier, E., Suetterlin, R., Hoemann, C. D., Aebi, U., and Buschmann, M. D. (2000) The Chondrocyte Cytoskeleton in Mature Articular Cartilage: Structure and Distribution of Actin, Tubulin, and Vimentin Filaments. *J. Histochem. Cytochem. 48*, 1307−1320.
(58) Cohen, S. I. A., Linse, S., Luheshi, L. M., Hellstrand, E., White, D. A., Rajah, L., Otzen, D. E., Vendruscolo, M., Dobson, C. M., and Knowles, T. P. J. (2013) Proliferation of amyloid-β42 aggregates occurs through a secondary nucleation mechanism. *Proc. Natl. Acad. Sci. U. S. A. 110*, 9758−9763.
(59) Knowles, T. P. J., Shu, W., Devlin, G. L., Meehan, S., Auer, S., Dobson, C. M., and Welland, M. E. (2007) Kinetics and thermodynamics of amyloid formation from direct measurements of fluctuations in fibril mass. *Proc. Natl. Acad. Sci. U. S. A. 104*, 10016−10021.
(60) Buell, A. K., Galvagnion, C., Gaspar, R., Sparr, E., Vendruscolo, M., Knowles, T. P. J., Linse, S., and Dobson, C. M. (2014) Solution conditions determine the relative importance of nucleation and growth processes in α-synuclein aggregation. *Proc. Natl. Acad. Sci. U. S. A. 111*, 7671−7676.
(61) Aprelev, A., Liu, Z., and Ferrone, F. A. (2011) The growth of sickle hemoglobin polymers. *Biophys. J. 101*, 885−891.
(62) Vekilov, P. G. (2007) Sickle-cell haemoglobin polymerization: is it the primary pathogenic event of sickle-cell anaemia? *Br. J. Haematol. 139*, 173−184.
(63) Chiti, F., and Dobson, C. M. (2006) Protein Misfolding, Functional Amyloid, and Human Disease. *Annu. Rev. Biochem. 75*, 333−366.
(64) Xu, L. Q., Wu, S., Buell, A. K., Cohen, S. I. A., Chen, L. J., Hu, W.-H., Cusack, S. A., Itzhaki, L. S., Zhang, H., Knowles, T. P. J., Dobson, C. M., Welland, M. E., Jones, G. W., and Perrett, S. (2013) Influence of specific HSP70 domains on fibril formation of the yeast prion protein Ure2. *Philos. Trans. R. Soc., B 368*, 20110410.

DOI: 10.1021/acs.biochem.8b00151
Biochemistry 2018, 57, 3641−3649